Constraints on the Physics of the Prompt Emission from Distant and Energetic Gamma-Ray Burst GRB 220101A

Alessio Mei[1,2] , Gor Oganesyan[1,2] , Anastasia Tsvetkova[3] , Maria Edvige Ravasio[4,5] , Biswajit Banerjee[1,2] ,
Francesco Brighenti[1], Samuele Ronchini[1,2] , Marica Branchesi[1,2] , and Dmitry Frederiks[3]
[1] Gran Sasso Science Institute, Viale F. Crispi 7, I-67100, L'Aquila (AQ), Italy; alessio.mei@gssi.it
[2] INFN—Laboratori Nazionali del Gran Sasso, I-67100, L'Aquila (AQ), Italy
[3] Ioffe Institute, Politekhnicheskaya 26, St. Petersburg 194021, Russia
[4] Department of Astrophysics/IMAPP, Radboud University, P.O. Box 9010, 6500 GL, Nijmegen, The Netherlands
[5] INAF—Astronomical Observatory of Brera, via E. Bianchi 46, I-23807 Merate, Italy

Abstract

The emission region of γ-ray bursts (GRBs) is poorly constrained. The uncertainty on the size of the dissipation site spans over 4 orders of magnitude (10^{12}–10^{17} cm) depending on the unknown energy composition of the GRB jets. The joint multiband analysis from soft X-rays to high energies (up to $\sim$1 GeV) of one of the most energetic and distant GRBs, GRB 220101A ($z = 4.618$), allows us to make an accurate distinction between prompt and early afterglow emissions. The enormous amount of energy released by GRB 220101A ($E_{\rm iso} \approx 3 \times 10^{54}$ erg) and the spectral cutoff at $E_{\rm cutoff} = 85^{+16}_{-26}$ MeV observed in the prompt emission spectrum constrain the parameter space of the GRB dissipation site. We put stringent constraints on the prompt emission site, requiring $700 < \Gamma_0 < 1160$ and $R_\gamma \sim 4.5 \times 10^{13}$ cm. Our findings further highlight the difficulty of finding a simple self-consistent picture in the electron–synchrotron scenario, favoring instead a proton–synchrotron model, which is also consistent with the observed spectral shape. Deeper measurements of the time variability of GRBs, together with accurate high-energy observations (MeV–GeV), would unveil the nature of the prompt emission.

Unified Astronomy Thesaurus concepts: Gamma-ray bursts (629)

1. Introduction

Despite many years of observations, the energy composition of γ-ray burst (GRB) jets and the dissipation processes responsible for the production of the prompt emission remain open mysteries (see, e.g., Piran 2004; Kumar & Zhang 2015, for a review). Models predicting the release of the prompt emission at the photosphere (e.g., Rees & Mészáros 2005; Pe'er 2008), via internal shocks (Rees & Meszaros 1994) or magnetic reconnection (e.g., Drenkhahn & Spruit 2002; Zhang & Yan 2011), are indistinguishable by using the current GRB observations.

Some GRB spectra have been successfully fitted by the slow-cooling (Tavani 1996) or the self-absorbed (Lloyd & Petrosian 2000) synchrotron model. Two components, a nonthermal plus a thermal component, have been invoked to explain time-resolved spectra of a few GRBs (Burgess et al. 2014; Yu et al. 2015), where an empirical function with fixed synchrotron spectral indices has been adopted. It was found, however, that GRB time-resolved and time-integrated spectra of GRBs can be well described by a single nonthermal emission component with a low-energy spectral break (Oganesyan et al. 2017, 2018; Ravasio et al. 2019) and corresponding spectral indices that are consistent with the marginally fast cooling regime of the synchrotron radiation. It was also shown that the realistic, physically derived synchrotron radiation model can account for GRB spectra in slow or marginally fast cooling regimes (Oganesyan et al. 2019; Burgess et al. 2020)[6] without the necessity to invoke additional

thermal components. However, some time-resolved spectra within a GRB are harder than predicted in the synchrotron radiation model (e.g., Acuner et al. 2020). While on one hand it seems difficult to assign the synchrotron origin to all the GRB spectra, on the other hand it is quite clear that the presence of the high-energy power-law segment in the GRB spectra requires nonthermal radiative processes to be present. Moreover, the exact regime of the radiation does not directly correspond to the unique dissipation model. For instance, single-shot accelerated electrons in low magnetized ejecta (Kumar & McMahon 2008; Beniamini & Piran 2013), reaccelerated electrons in highly magnetized ejecta (Gill et al. 2020), or protons in the magnetically dominated jets (Ghisellini et al. 2020) can produce the very same marginally fast cooling synchrotron spectra. Therefore, more specific observational inputs are required to discriminate between GRB jet dissipation models.

Regardless of the dominant radiative processes responsible for the GRB production, there should be a critical energy in the GRB spectrum above which the photons are suppressed by the pair production (Ruderman 1975; Piran 1999). The localization of the high-energy spectral cutoff $E_{\rm cutoff}$ enables us to constrain the size of the jet R_γ as a function of the bulk Lorentz factor Γ_0 where the prompt emission is produced (Lithwick & Sari 2001; Granot & Cohen-Tanugi 2008; Gupta & Zhang 2008; Zhang & Pe'er 2009; Hascoët et al. 2012; Vianello et al. 2018; Chand et al. 2020). Given the large typical $\Gamma_0 \geqslant 100$ (Ghirlanda et al. 2018), the resulting observed spectral cutoff is $E_{\rm cutoff} \geqslant (51\,{\rm MeV})\,\Gamma_{0,2}\,(1 + z)^{-1}$. At these energies, the identification of the cutoff faces two complications: the extremely low instrumental response of operating GRB detectors, and the presence of an afterglow emission that typically overshines the prompt emission at

---

[6] A more complete list of references, including empirical and physical modeling of single GRB spectra, can be found in Zhang (2020).

Table 1
Best-fit Parameters Obtained from the Time-resolved Independent Spectral Analysis of the XRT, BAT+GBM+KW, and LAT Data Sets

Time Bin (s)	Instruments	Flux (10^{-7} erg s^{-1} cm^{-2})	α	β	E_{ch} (keV)	Significance
93 − 102	BAT+GBM+KW	33.60 ± 5.03	$-0.60^{+0.06}_{-0.06}$	$-1.99^{+0.07}_{-0.09}$	$171.94^{+22.56}_{-19.60}$	Stat/dof = 1.22
	XRT	0.23 ± 0.02	$-0.92^{+0.10}_{-0.10}$	//	//	Stat/dof = 302.25/426
	LAT	0.03 ± 0.02	//	-2.60 ± 0.74	//	TS = 20
102 − 110	BAT+GBM+KW	26.80 ± 3.12	$-0.58^{+0.05}_{-0.05}$	$-2.30^{+0.10}_{-0.12}$	$204.54^{+22.28}_{-19.69}$	Stat/dof = 1.01
	XRT	0.27 ± 0.03	$-0.92^{+0.10}_{-0.11}$	//	//	Stat/dof = 332.48/505
	LAT	0.30 ± 0.13	//	-5.36 ± 1.68	//	TS = 28
110 − 118	BAT+GBM+KW	14.60 ± 1.27	$-0.60^{+0.04}_{-0.04}$	$-3.09^{+0.28}_{-0.42}$	$172.95^{+15.21}_{-13.14}$	Stat/dof = 1.16
	XRT	0.28 ± 0.03	$-0.85^{+0.10}_{-0.10}$	//	//	Stat/dof = 384.71/450
	LAT	0.21 ± 0.08	//	-3.81 ± 0.99	//	TS = 18
118 − 134	BAT+GBM+KW	2.61 ± 0.18	$-0.97^{+0.04}_{-0.08}$	$-9.33^{+19.33}_{-9.33}$	$160.40^{+30.98}_{-19.59}$	Stat/dof = 0.91
	XRT	0.19 ± 0.01	$-1.30^{+0.08}_{-0.08}$	//	//	Stat/dof = 452.61/559
	LAT	0.25 ± 0.13	//	-3.62 ± 1.22	//	TS = 17
134 − 142	BAT+GBM+KW	1.18 ± 0.80	$-0.79^{+0.39}_{-0.33}$	$-2.34^{+0.41}_{-2.34}$	$78.06^{+88.87}_{-30.80}$	Stat/dof = 1.50
	XRT	0.12 ± 0.01	$-1.80^{+0.11}_{-0.11}$	//	//	Stat/dof = 296.04/448
	LAT	0.19 ± 0.09	//	-2.33 ± 0.59	//	TS = 24
142 − 159	BAT+GBM+KW	0.71 ± 0.68	$-1.44^{+0.20}_{-0.08}$	$-9.96^{+19.96}_{-9.96}$	$540.28^{+3048.23}_{-307.37}$	Stat/dof = 0.93
	XRT	0.12 ± 0.01	$-1.85^{+0.08}_{-0.08}$	//	//	Stat/dof = 366.27/454
	LAT	0.35 ± 0.17	//	-3.39 ± 0.99	//	TS = 32

Note. We fit XRT and LAT data with a power law, whereas we fit BAT+GBM+KW with the Band model. We report the fluxes integrated over the respective instrument energy band; the low- and high-energy photon indexes α and β, respectively; and the Band characteristic energy E_{ch}. Errors are reported with 1σ confidence level.

0.1–10 GeV for the majority of the GRBs detected by Fermi/LAT (see Nava 2018, for a review). We analyze the broadband data from soft X-rays (0.5–10 keV) to high energies (∼1 GeV) of GRB 220101A, one of the most energetic GRBs ($E_{\text{iso}} \approx 3 \times 10^{54}$ erg), located at very high redshift ($z = 4.618$) and detected by the X-Ray Telescope (XRT, 0.5–10 keV) and Burst Alert Telescope (BAT; 15–150 keV) on board the Neil Gehrels Swift Observatory (Swift), the Gamma-ray Burst Monitor (GBM; 8 keV–40 MeV) and Large Area Telescope (LAT; 100 MeV–300 GeV) on board the Fermi satellite, and the Konus-Wind (KW; ∼20 keV–20 MeV) instrument, together with several optical instruments. We identify the high-energy spectral cutoff and place the most stringent constraints on the R_γ–Γ_0 plane. These constraints are fully consistent with the limits obtained from the optical-to-GeV afterglow emission modeled by the dissipation of the jet in the circumburst medium (Paczynski & Rhoads 1993). We discuss the physical implications of our findings and stress the necessity of better early MeV–GeV observations.

2. Independent Spectral Analysis

We perform a multi-instrumental spectral and temporal analysis, using the HEASARC package XSPEC[7] and the Fermi Science tool GTBURST.[8] Details on data retrieving and reduction methods for all the instruments used in this work are reported in Appendix A.

Initially, we divide the data set into three blocks: XRT, LAT, and BAT+GBM+KW data. For each block, we perform a time-resolved analysis, where the choice of the time bins is driven by the time intervals where the Fermi/LAT emission

reaches a test statistic TS > 10. XRT is fitted through XSPEC with a power-law model, powerlaw in XSPEC notation, taking into account the Tuebingen–Boulder interstellar dust absorption ($N_{\text{H}} = 0.063 \times 10^{22}$cm^{-2}) and host galaxy dust absorption (source redshift $z = 4.618$) by using the XSPEC models tbabs and ztbabs, respectively. All the XRT spectra are consistent with zero intrinsic absorption. LAT spectra are also fitted with a power law through GTBURST. BAT, GBM, and KW spectra are jointly fitted through XSPEC with a Band model (Band et al. 1993), grbm in XSPEC notation, multiplied by cross-calibration constants. The results of these fits are reported in Table 1, while in Figure 1 we show light curves and photon indexes from the time-resolved spectral analysis.

From the bottom panel of Figure 1 we notice that in the time bins at $t > 118$ s both XRT and LAT spectra start to deviate from a single nonthermal component, i.e., the prompt emission spectrum. For this reason, we introduce two new time bins, one between 94 and 118 s after the burst (hereafter *prompt* time bin) and the other between 118 and 241 s after the burst (hereafter *prompt+afterglow* time bin), and we perform the same analysis of the previous time bins.

In the *prompt* time bin, XRT and LAT photon spectra can be described, respectively, by $N_{\text{XRT}} \propto E_{\text{XRT}}^{-0.8}$ and $N_{\text{LAT}} \propto E_{\text{LAT}}^{-4.4\pm0.9}$, both consistent with the low- and high-energy slopes inferred by fitting BAT+GBM+KW data. Conversely, in the *prompt+afterglow* time bin, we observe an excess in the spectrum at low and high energies, which leads to softer/harder slopes in XRT and LAT power laws (Figure 1, top panels). In particular, XRT and LAT spectra are best fitted by $N_{\text{XRT}} \propto E_{\text{XRT}}^{-1.90}$ and $N_{\text{LAT}} \propto E_{\text{LAT}}^{-2.1\pm0.3}$. This is indicative of a dominance of the keV-to-MeV (up to ∼0.25 GeV) prompt emission at early times, while at later times an additional component arises. We interpret
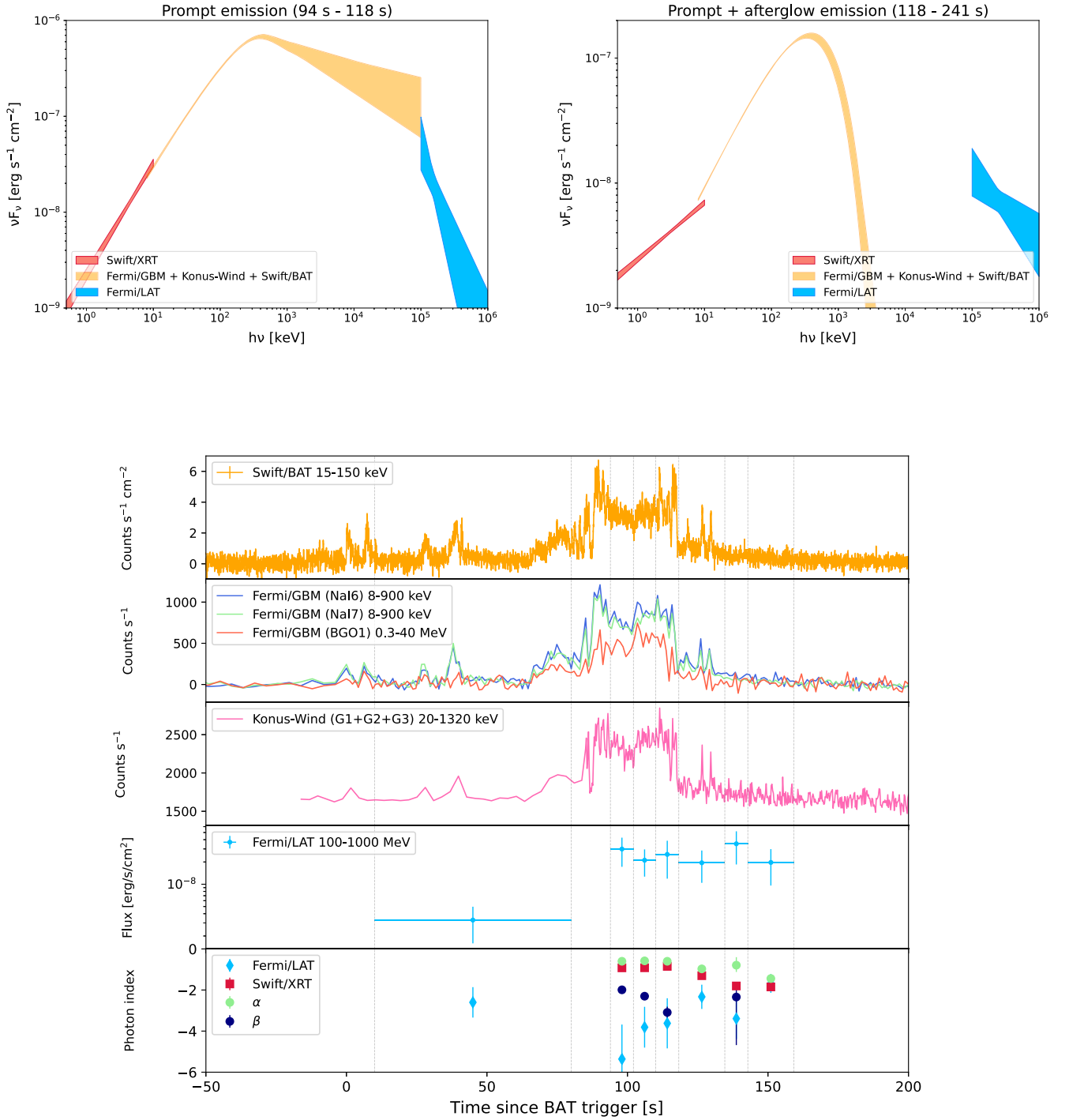
Figure 1. Top panel: modeled spectra considering three independent data sets: XRT (in red), BAT+GBM+KW (in orange), and LAT (in blue). The models are shown in the νF_ν representation. Two distinguished time epochs are chosen: the first one dominated fully by the prompt emission (94–118 s; on the left), and the second one (118–241 s; on the right) with the separate prompt emission (8 keV–100 MeV) and afterglow components (in X-rays and high energies). We show the energy-dependent flux uncertainty regions ("butterflies") derived from Swift/XRT and Fermi/LAT data analysis in red and blue, respectively. Bottom panel: Swift/BAT (15–150 keV), Fermi/GBM (8 keV–40 MeV), and KW (13–750 keV) count rate light curves; Fermi/LAT flux light curve (0.1–1 GeV); and photon indices measured from the Swift/XRT (0.5–10 keV) and Fermi/LAT (0.1–1 GeV) time-resolved spectra.

this component to be afterglow emission from an external jet dissipation (Paczynski & Rhoads 1993; Mészáros & Rees 1997).

3. Joint Spectral Analysis

The independent spectral analysis of three data blocks suggests the rise of a second emission component together with the prompt emission at times $t > 118$ s. In order to further

investigate this scenario, we perform a joint spectral analysis by fitting the XRT, BAT, GBM, KW, and LAT spectra through XSPEC. To take into account the differences among the instruments, we use cross-calibration constants and a mixed likelihood approach to weight correctly data errors (e.g., Ajello et al. 2020), with different statistics depending on the instrument (PGstat for Fermi/GBM; Cstat for Fermi/LAT, Swift/XRT, and KW; Gaussian statistics for Swift/BAT).

3.1. Prompt Emission from X-Rays to High Energies

Initially, we fit the joint spectra in the *prompt* time bin with a Band function. We account for the galactic absorption, and we fix the extragalactic absorption to zero, as evidenced by the previous independent analysis. We also compute the flux in the band 0.1 keV–0.25 GeV through the XSPEC model cflux, since the most energetic LAT photon has an energy of ∼250 MeV in this particular time bin.

We introduce an exponential cutoff at high energies, described in XSPEC by the model component highecut. The overall model (hereafter *Band+cutoff*) includes two new parameters: the energy at which the cutoff starts to modify the base spectrum, E_c, and the energy that regulates the sharpness of the decay, E_{fold}. The sum of these two quantities provides the energy at which the flux drops by a factor $1/e$, namely $E_{cutoff} = E_c + E_{fold}$. We test different E_c values and find consistent results on E_{cutoff}, implying that the position of the E_c energy does not affect the main results of the analysis. Therefore, we fix $E_c = 5$ MeV in order to minimize the number of free parameters. The results are shown in Figure 2.

To select which model fits better the data, we use the likelihood ratio test (LRT). We define m_0 as the null model, in this case the simple Band model, and m_1 as the alternative model, in this case the more complex *Band+cutoff* model. We want to estimate whether m_1 fits the data better than m_0 by computing the ratio between their mixed likelihoods L_0/L_1. We define the test statistics TS $= -2\log(L_0/L_1)$ and use it as a best-fit indicator. If TS > 0, then $L_1 > L_0$, which means that the fit improves by using model m_1 instead of m_0.

The data we used for the spectral analysis in the *prompt* time bin do not meet the regularity conditions required by Wilks's theorem (see Algeri et al. 2020). Therefore, to assess whether the improvement is statistically significant, we simulate 10^3 spectra for each instrument employed in the joint spectral analysis, using as input the null model m_0 and its best-fit parameters obtained from the real data fit. Then, we fit all the simulated spectra with both m_0 and m_1 and compute the relative test statistics TS_{sim}. From the TS distribution we compute the probability density function using the kernel density estimator. To reject the null hypothesis, we require that the *p*-value, associated with the TS estimated from real data, is lower than a threshold $\alpha = 0.01$.

From the real data fit, we measure $TS_{real} = 10$, which corresponds to a *p*-value of $p = 2 \times 10^{-7}$, allowing us to reject the null hypothesis, implying that the addition of an exponential cutoff (*Band+cutoff*) fits significantly better the spectral data with respect to the simple Band model. In Figure 3 we show the probability density for different test statistics obtained by fitting 10^3 fake spectra.

The best-fit parameters of the *Band+cutoff* model are $\alpha = -0.78^{+0.02}_{-0.02}$, $\beta = -2.18^{+0.06}_{-0.08}$, $E_{peak} = (316 \pm 20)$ keV, $E_{cutoff} = 85^{+16}_{-26}$ MeV, and $F_{0.1keV-0.25GeV} = (2.96 \pm 0.09) \times 10^{-6}$ erg s^{-1} cm^{-2}.

We produce marginalized posterior distributions of the spectral parameters through the XSPEC command chain (see Appendix B.1).

3.2. Modeling of the Afterglow Light Curve

We use data provided by XRT (130 s to 6×10^5 s) and LAT (118–160 s, three time bins) and the *r*-filter optical data to infer the parameters of the external shock. First, we fit the X-ray light curve empirically by a smoothed broken power law, which returns $F_X \propto t^{-0.98\pm0.01}$ before the temporal break of $t_X \approx 3 \times 10^4$ s and $F_X \propto t^{-1.7\pm0.1}$ after. This temporal behavior is in the best match with the forward shock propagating in the homogeneous circumburst medium by requiring that the electron distribution index $p > 2$ (Sari et al. 1998; Granot & Sari 2002; Gao et al. 2013). The temporal break in this scenario corresponds to the jet break, thus allowing us to constrain the opening angle of the jet once the density of the circumburst medium and the kinetic energy of the jet are established. To get constraints on the jet opening angle, the density of the medium, and the microphysical parameters of the external shock, we model the joint optical-to-GeV light curve by the standard forward shock model in the homogeneous circumburst medium. Since we observe the afterglow in the decaying phase (no peak is observed) and deal with one of the most energetic GRBs (i.e., observed on-axis), we safely use the analytical expressions for the self-similar adiabatic solutions (Granot & Sari 2002; Gao et al. 2013). We sample all six parameters via Markov Chain Monte Carlo (MCMC), namely the isotropic equivalent kinetic energy of the jet E_{kin}, the opening angle of the jet θ_j, the circumburst medium density n, electron distribution index p, and constant fraction of the shock energy that goes into electrons ϵ_e and into the magnetic energy density ϵ_B. We include also one more parameter, the unknown absorption of the optical emission A_R.

We explain the details of the MCMC in Appendix B.2. The priors used for the MCMC analysis, together with the results of the fit, are reported in Table 2. Figure 4 shows the optical, X-ray, and high-energy light curves at $t > 118$ s with the relative best-fit models.

4. Constraints on the Prompt Emission Region

4.1. Limits from the Afterglow Emission

The weakest lower limit on the bulk Lorentz factor can be obtained requiring that the highest energy of the photons observed during the afterglow emission cannot exceed the maximum synchrotron frequency emitted by electrons in the jet comoving frame $h\nu_{max} = hm_ec^3/2\pi^2e^2 \simeq 22$ MeV (Guilbert et al. 1983). Given the maximum energy of the photon $E_{LAT,max} = 930$ MeV detected by Fermi/LAT at 150 s, we place the lower limit on the bulk Lorentz factor of

$$\Gamma_0 > \Gamma_{burn-off} = \frac{E_{LAT,max}}{h\nu_{max}}(1 + z) \simeq 237. \qquad (1)$$

One should pay attention to this limit, since larger $h\nu_{max}$ can be obtained in the shock-accelerated electrons if the magnetic field is much stronger close to the shock front and decays downstream (Kumar et al. 2012). However, in our case the further lower limit on Γ_0 exceeds $\Gamma_{burn-off}$; therefore, our general conclusions do not depend on the details of the magnetic field profile in the shock front.

Another lower limit on the bulk Lorentz factor can be found by the fact that we do not witness the peak of the afterglow emission (Sari & Piran 1999). The upper limit on the peak time of the afterglow emission $t_p < 118$ returns then the lower limit on Γ_0 (Ghisellini et al. 2010; Ghirlanda et al. 2012; Lü et al.
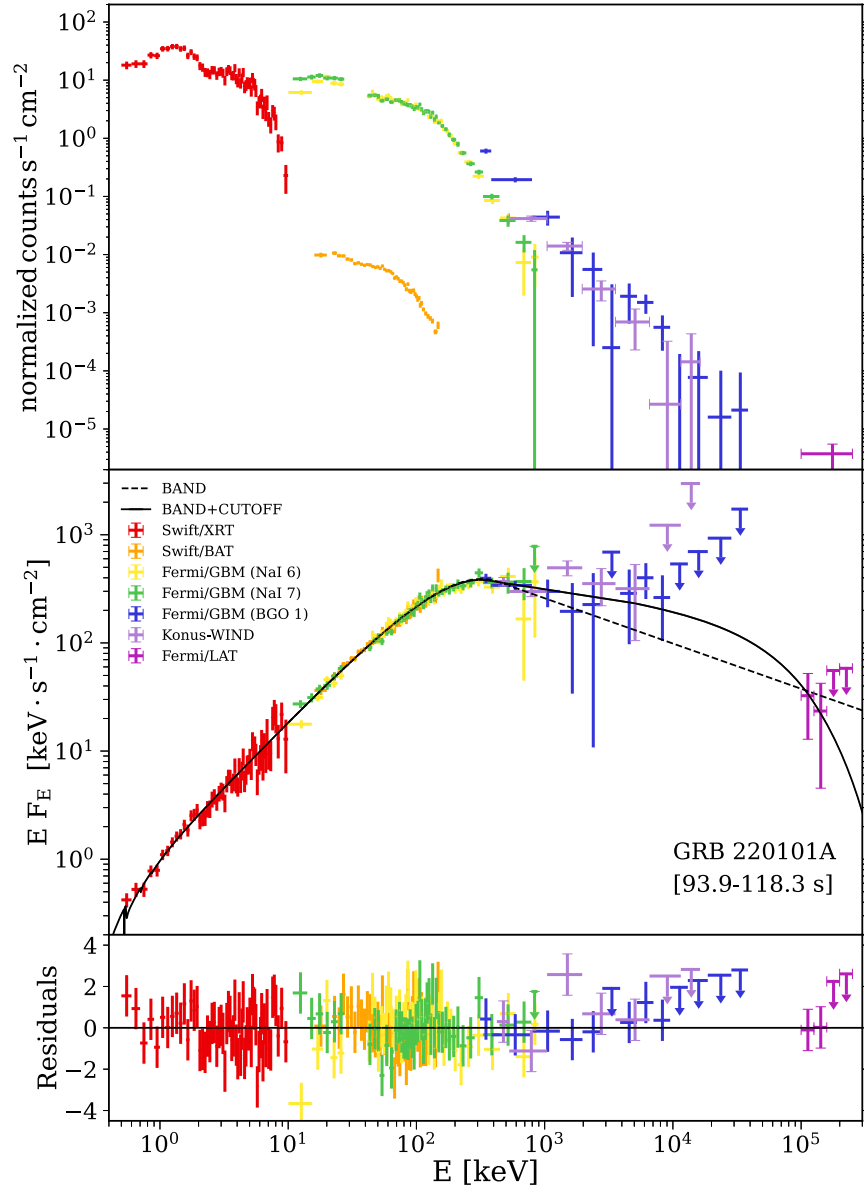
Figure 2. The joint X-ray to high-energy spectrum of GRB 220101A at 94–118 s modeled by the Band function with the high-energy spectral cutoff $E_{\rm cutoff}$ (*Band +cutoff*). We show the spectrum in the count representation (top panel), that in the spectral energy density representation (SED; middle panel), and the residuals between the data and best-fit model (bottom panel). We show the data points and relative errors with different colors, depending on the instruments, while the 3σ upper limits are shown with arrow markers. The joint Band model fit is shown with a black dashed line.

2012; Nava et al. 2013):

$$\Gamma_0 > \Gamma_{\rm decl.} = k \left(\frac{E_{\rm kin}}{n m_p c^5} \right)^{\frac{1}{8}} t_p^{-\frac{3}{8}}, \qquad (2)$$

where k is the normalization factor adopted from Nava et al. (2013).

4.2. The Compactness Argument

Constraints on the R_γ–Γ_0 parameter space can be obtained from the compactness argument, which relies only on the prompt emission properties. In the comoving frame of the jet, high-energy photons produce pairs. The optical depth to the pair production of a photon with energy ϵ' (measured in the jet

comoving frame) is defined as

$$\tau_{\gamma\gamma}(\epsilon') = \eta(\beta_e) \sigma_T \frac{U'_{\rm rad}(1/\epsilon')}{m_e c^2} \delta R', \qquad (3)$$

where $U_{\rm rad}'$ is the comoving photon energy density, $\delta R' \approx R_\gamma/\Gamma_0$ is the comoving width of the jet shell, $\eta(\beta_e) = (7/6) \cdot (2 + \beta_e)^{-1}(1 + \beta_e)^{-5/3}$, and β_e is the energy spectral index of the observed GRB spectrum (Svensson 1987). To infer the R_γ–Γ_0 relation for a given observable ($E_{\rm cut}$, spectral indices, and the peak energy of the GRB spectrum $E_{\rm peak}$), one can use either the total radiated energy of the single pulse $E_{\rm rad}$ or its luminosity $L_{\rm rad}$ to define $U_{\rm rad}'(1/\epsilon')$. If $E_{\rm rad}$ is used, then $\tau_{\gamma\gamma} \propto E_{\rm rad}/R_\gamma^2$, whereas if $L_{\rm rad}$ is adopted, the dependence is $\tau_{\gamma\gamma} \propto L_{\rm rad}/(R_\gamma \Gamma_0^2)$. Naturally, the difference in $\tau_{\gamma\gamma}$ for a γ-ray flash observed in the lab frame is a factor of $R_\gamma/c\Gamma_0^2$. However,
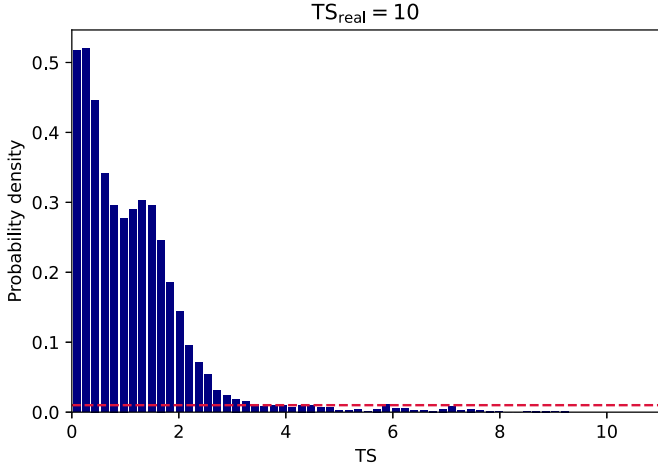
Figure 3. Distribution of simulated test statistics, obtained by fitting 10^3 fake spectra during the *prompt* time bin (930–118 s) with Band (null model) and *Band+cutoff* (alternative model). Fake spectra are produced by using as an input the Band model and its relative best-fit parameters obtained from the fit of the real data. The red dashed line represents a probability density of 0.01.

Table 2
Mean Posterior Values of the Afterglow Model Parameters Considering XRT and LAT Data

MCMC Parameter	Prior	Before LAT Cut	After LAT Cut
$\log E_{\rm kin}$ (erg)	(50, 60)	$56.54^{+1.24}_{-1.01}$	$56.63^{+1.03}_{-0.95}$
$\log n$ (cm^{-3})	(−4, 4)	$1.58^{+1.76}_{-2.66}$	$-1.11^{+2.35}_{-1.98}$
θ_j (deg)	(0.1, 10)	$1.31^{+1.08}_{-0.70}$	$0.63^{+0.54}_{-0.24}$
p	(2, 2.5)	$2.005^{+0.006}_{-0.003}$	$2.006^{+0.005}_{-0.003}$
$\log \epsilon_e$	(−4, −0.5)	$-1.85^{+0.96}_{-1.31}$	$-1.99^{+0.94}_{-1.12}$
$\log \epsilon_B$	(−8, −0.5)	$-4.38^{+1.83}_{-1.15}$	$-2.57^{+1.46}_{-1.75}$
A_R	(0, 3)	$2.05^{+0.09}_{-0.08}$	$2.06^{+0.10}_{-0.08}$
Derived Parameter			
$\log E_{{\rm kin},\theta}$ (erg)		$52.93^{+1.09}_{-0.93}$	$52.31^{+1.33}_{-0.85}$
$\log E_{\gamma,\theta}$ (erg)		$50.92^{+0.52}_{-0.67}$	$50.29^{+0.54}_{-0.42}$
η_γ		<0.09	<0.07
$\Gamma_{\rm transp}$		7554	7090
$\Gamma_{\rm LAT}$			1270
$\Gamma_{\rm cut}$			1567
$\Gamma_{\rm decl.}$			578

Note. We also report parameter values derived from afterglow MCMC analysis, namely the angle-corrected kinetic energy $E_{{\rm kin},\theta}$, the angle-corrected energy $E_{\gamma,\theta}$ emitted in the prompt phase, the relative energy conversion efficiency η_γ, and upper/lower limits on Γ_0 ($\Gamma_{\rm transp}$, $\Gamma_{\rm LAT}$, $\Gamma_{\rm cut}$, $\Gamma_{\rm decl.}$). All the estimates in this table are reported before and after cutting the posterior according to the LAT limit on coasting and deceleration afterglow phases. Errors and upper/lower limits are computed at the 1σ credible region.

we do use the spectrum in the *prompt* time bin to constrain the high-energy spectral cutoff; therefore, $L_{\rm iso}$ is the best proxy for $L_{\rm rad}$, whereas using $E_{\rm iso}$ instead of $E_{\rm rad}$ would overestimate the optical depth by the factor $T_{\rm dur} c \Gamma_0^2 / R_\gamma$, i.e., by 2–3 orders of magnitude, where $T_{\rm dur}$ is the time required for the spectral analysis. We notice that some works use $rmE_{\rm iso}$ as a proxy for $E_{\rm rad}$ (Gupta & Zhang 2008; Zhang & Pe'er 2009), while others adopt $L_{\rm iso}$ as a proxy for $L_{\rm rad}$ (Lithwick & Sari 2001; Granot & Sari 2002). Alternatively, one can use $E_{\rm iso}$ as an approximation
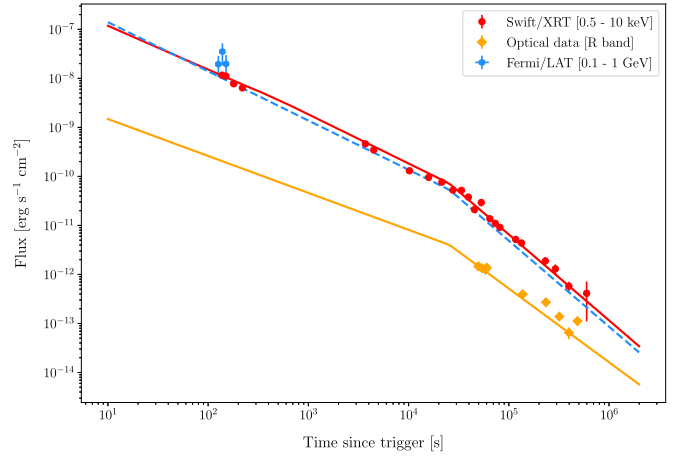

Figure 4. Optical (*r* band; in orange), X-ray (0.5–10 keV; in red), and high-energy (0.1–1 GeV; in blue) light curves of GRB 220101A. Lines correspond to the afterglow model by the propagation of the forward shock in a homogeneous circumburst medium. Early X-ray (<134 s) and high-energy data (<118 s) are not considered for the modeling of the joint light curves.

for $E_{\rm rad}$, but it requires a correction factor of $t_{\rm var}/T_{\rm dur}$, where $t_{\rm var}$ is the variability timescale (Hascoët et al. 2012).

Knowing that $E_{\rm cutoff} \simeq 80$ MeV in the observer reference frame, we can obtain an upper limit for Γ_0 by comparing $E_{\rm cutoff}$ in the observer and source reference frames:

$$\Gamma_0 < \Gamma_{\rm cut} = \frac{E_{\rm cutoff}}{m_e c^2}(1 + z). \qquad (4)$$

Given the measured isotropic equivalent luminosity $L_{\rm iso}$ between 94 and 118 s, the GRB peak energy $E_{\rm peak}$, energy spectral indices α_e and β_e, and the spectral cutoff $E_{\rm cutoff}$, by imposing $\tau_{\gamma\gamma} = 1$ we can derive a relation between R_γ and Γ_0 (M. E. Ravasio et al. 2022, in preparation):

$$R_\gamma = \eta(\beta_e)\sigma_T \frac{L_{\rm iso}}{4\pi} \frac{(1 - \alpha_e)(\beta_e - 1)}{\beta_e - \alpha_e} \left(\frac{(m_e c^2)^2}{E_{\rm peak}} \right)^{-\beta_e}$$

$$\times \frac{E_{\rm cutoff}^{\beta_e}}{c E_{\rm peak}} \Gamma_0^{-2-2\beta_e}. \qquad (5)$$

In this equation, both $E_{\rm peak}$ and $E_{\rm cutoff}$ are corrected for the redshift.

4.3. Upper Limit on Γ_0 from the Fireball Dynamics

In the hot fireball model, by requiring that the GRB production site is above the jet photosphere, i.e., $R_\gamma > R_{\rm ph}(\Gamma_0)$, one can obtain the following upper limit on Γ_0:

$$\Gamma_0 < \Gamma_{\rm transp} = \left(\frac{L_{\rm iso}\sigma_T}{8\pi m_p c^3 \eta_\gamma r_0} \right)^{1/4}, \qquad (6)$$

where $\eta_\gamma = E_{\rm iso}/(E_{\rm iso} + E_{\rm kin})$ is the efficiency of the prompt emission production and $r_0 \sim 10$ km is the initial fireball radius, which is of order of the central engine one (Daigne & Mochkovitch 2002).

4.4. Upper Limit on Γ_0 from the High-energy Afterglow Emission

The early rise of the forward shock emission at high energies, quantified by the observed fluence $S_{\text{HE,rise}}$ in the energy band 0.1–1 GeV, strongly depends on the bulk Lorentz factor as $S_{\text{HE,rise}} \propto \Gamma_0^{2p+4}$. Similarly, before the jet starts to decelerate, at the peak of the afterglow emission, the observed high-energy afterglow fluence $S_{\text{HE,peak}}$ depends on the observed prompt fluence S_{iso} and on its efficiency η_γ as $S_{\text{HE,peak}} \propto \frac{1-\eta_\gamma}{\eta_\gamma} S_{\text{iso}}$ (Nava et al. 2017). These relations are based on two assumptions: first, the high-energy afterglow emission corresponds to the synchrotron emission above the cooling frequency ν_c (Kumar & Duran 2010); and, second, the inverse Compton (IC) cooling of electrons above ν_c is above the Klein–Nishina limit for the typical parameters of the external shock of GRBs (Beniamini et al. 2015).

We observe that the sub-GeV emission at early times is dominated by prompt emission (Figure 1, top left panel). In addition, from the modeling of the high-energy afterglow light curve (Figure 4), we infer that the coasting and deceleration phases take place before ∼100 s from the burst, simultaneously with prompt emission. This implies that, in the prompt time bin (94–118 s), high-energy afterglow fluence at coasting and deceleration phases cannot exceed the observed high-energy prompt emission $S_{\text{HE,prompt}}$ in the same time bin. Therefore, by requiring that both $S_{\text{HE,rise}}$ and $S_{\text{HE,peak}}$ are smaller than $S_{\text{HE,prompt}}$, we can not only find a new constraint for $\Gamma_0 < \Gamma_{\text{LAT}}$ but also perform a cut on the posterior distributions obtained from the afterglow light-curve modeling. The new posterior distributions lead to more precise afterglow parameter estimates, thus improving the other upper/lower limits on Γ_0.

To take into account the additional electron cooling by the IC, we assume the fast-cooling mode of the synchrotron radiation, i.e., $Y \approx (\epsilon_e/\epsilon_B)^{1/2}$, and we correct it for the Klein–Nishina effect (Nakar et al. 2009).

One could think of an alternative scenario, where the GeV afterglow emission is absorbed by the MeV prompt emission produced below the afterglow deceleration radius (Zou et al. 2011). In that case, the fact that we do not observe bright GeV afterglow emission is due to the prior MeV–GeV prompt-to-the-afterglow photon absorption. However, in that case we would require the total energy of the prompt emission to be much more than what we have observed, since we observe a high-energy power law in the prompt emission spectrum. Dealing with one of the most energetic GRBs, we disfavor this scenario.

4.5. R_γ–Γ_0 Constraints

We develop a method to constrain the allowed parameter region in the R_γ–Γ_0 plane for GRB 220101A. The method consists in building a Γ_0 parameter distribution based on the previous prompt and afterglow analyses (Section 3), together with the Γ limits discussed in Section 4. By randomly sampling $N = 8 \times 10^5$ times the posterior distributions of prompt spectral parameters (F, α, β, E_{ch}, E_{cutoff}) and of the afterglow parameters (E_{kin}, θ_j, n, p, A_r, ϵ_e, ϵ_B) previously obtained (see Appendix B for details), we can build distributions also for the Γ limits (Γ_{transp}, Γ_{LAT}, Γ_{cut}, $\Gamma_{\text{decl.}}$). Once the conditions for Γ_0 are obtained, we impose its distribution to be uniform and restricted by the Γ limits. This new distribution, together with the spectral parameter ones, is sampled again in order to obtain

N estimates of R_γ, by requiring that $\tau_{\gamma\gamma} = 1$ at E_{cutoff} (Equation (5)). At the end of these steps, we can define two distributions for R_γ and Γ_0, whose values will occupy a given restricted region of the parameter space depending on the conditions imposed on Γ_0. The more constraints we use, the smaller this region is, and hence the more precise is the estimate of these values. Therefore, we present three scenarios where we take into consideration different conditions, in order to highlight the role of each observational feature. We report constraints and upper and lower limits with a 1σ confidence level, i.e., computing the 50th, 84th, and 16th percentiles of the parameter distribution, respectively.

In the first scenario, we only consider the condition on fireball dynamics, providing a wide flat distribution for Γ_0 in the range between 1 and Γ_{transp}. This returns $\log R_\gamma[\text{cm}] > 10$ and $\Gamma_0 < 6343$.

In the second scenario, we add the condition derived from LAT observation in both prompt and afterglow emissions. We take $\Gamma_{\text{burn−off}}$ as the lower limit for Γ_0 and the minimum between Γ_{cut}, Γ_{LAT}, and Γ_{transp} as the upper limit. We obtain $\log R_\gamma[\text{cm}] = 14.09^{+1.22}_{-0.73}$ and $400 < \Gamma_0 < 1100$.

We compute upper/lower limits in this and the following steps after performing a cut in the afterglow posterior distributions. We define an initial Γ_0 uniformly distributed between $\Gamma_{\text{burn−off}}$ and the Γ_{transp} estimate from the previous step. Afterward, we sample the initial posteriors and accept the values of Γ_0 and prompt/afterglow parameters that satisfy the conditions $S_{\text{HE,rise}} < S_{\text{HE,prompt}}$ and $S_{\text{HE,peak}} < S_{\text{HE,prompt}}$. We define Γ_{LAT} as the maximum value of the Γ_0 distribution after the LAT cut. We report the 1σ values of afterglow and derived parameters after the posterior cut in Table 2.

In the third scenario, we add the condition on the deceleration phase in the X-ray afterglow observed by Swift/XRT. Therefore, we define the maximum between $\Gamma_{\text{decl.}}$ and $\Gamma_{\text{burn−off}}$ as the lower limit on Γ_0 and the minimum between Γ_{LAT}, Γ_{transp}, and Γ_{cut} as the upper limit. The Γ limit posteriors are considered after the LAT cut. We obtain $\log R_\gamma[\text{cm}] = 13.7^{+0.6}_{-0.4}$ and $700 < \Gamma_0 < 1160$.

In Figure 5 we show how the initial parameter space is reduced after taking into consideration all the conditions on Γ_0. We notice that the most stringent conditions are the ones obtained by forward shock deceleration from the X-ray afterglow light curve and by the high-energy spectral cutoff during prompt emission.

5. Discussion and Conclusions

Given the values of $R_\gamma \approx 4.5 \times 10^{13}$ cm and the median $\Gamma_0 \approx 900$, we can provide an estimate of the magnetic field B' (in the comoving frame) that matches the observed peak energy of the GRB spectrum $E_{\text{peak}} \approx 300$ keV, assuming that the dominant radiative process is synchrotron emission. In addition, we assume $\nu_c \simeq \nu_m$, since the low-energy spectral index α is roughly consistent with the usual value of $-2/3$ and we do not observe any additional spectral break. If we consider the electrons to produce the observed spectrum, we require

$$B'_e \approx (190 \text{ G}) \, R_{13.65}^{-2/3} \, \Gamma_{0,900} \, h\nu_{\text{obs,300}}^{-1/3}. \tag{7}$$

In this estimate we consider that the synchrotron cooling timescale coincides with the angular and radial timescales, i.e., $t_{\text{syn}} = t_R = t_\theta = R/2c\Gamma_0^2$.
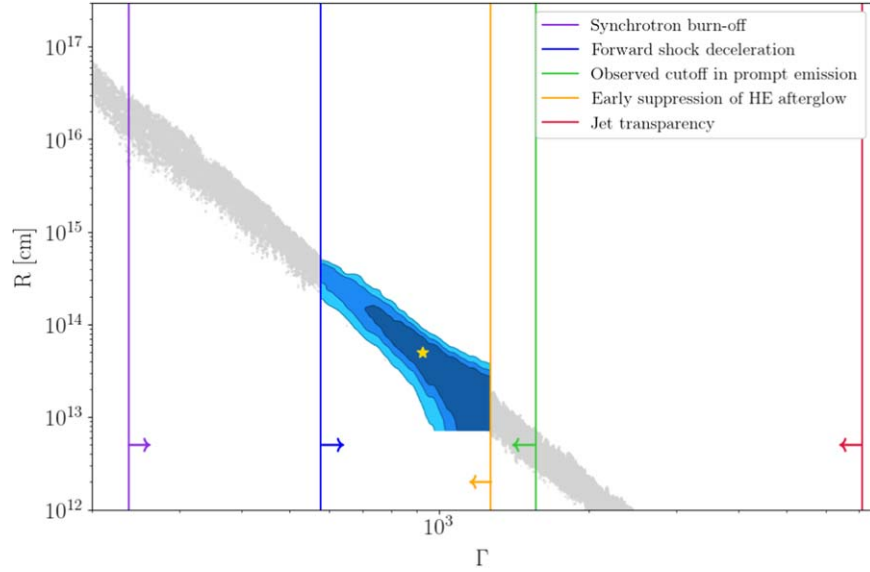
Figure 5. Constraints on the R_γ–Γ_0 prompt emission region. The gray points are drawn from the R_γ–Γ_0 distribution after considering only the condition on the cutoff (first scenario), corresponding to the allowed parameter space derived from the opacity argument (requiring $\tau_{\gamma\gamma} = 1$ at E_{cutoff}). We show the lower limits on Γ_0 from the maximum synchrotron emitted energy (purple line) and from external shock deceleration (blue line) and the upper limits on Γ_0 from the cutoff observation in prompt emission (green line), GeV afterglow emission at coasting and deceleration phase (orange line), and jet transparency requirement (red line). These upper/lower limits are reported with a 1σ confidence level. The blue shaded areas correspond to the R_γ–Γ_0 parameter contours at 1σ, 2σ, and 3σ confidence levels. The contour plot and relative 1σ estimate of R_γ and Γ_0 (in yellow) are both obtained in the last scenario, which takes into account all the conditions on R_γ–Γ_0 parameters.

For such low values of the magnetic field and the luminosity observed, the radiation energy density in the emitting region could imply a nonnegligible synchrotron self-Compton (SSC) cooling of the particles (Ghisellini et al. 2020). An electron–synchrotron component driven by a small magnetic field $B'_e \approx 190\,\mathrm{G}$ in a relatively compact emitting region ($R_\gamma \approx 4.5 \times 10^{13}\,\mathrm{cm}$) would be easily overshined by the SSC emission (of at least a factor 10^4), not matching the spectral behavior observed in this source (Kumar & McMahon 2008; Beniamini & Piran 2013; Oganesyan et al. 2019; Ghisellini et al. 2020).

This tension can be alleviated if one considers protons as synchrotron emitters in prompt emission. In fact, protons can naturally produce marginally fast cooling synchrotron spectra, allowing for large magnetic fields of the order of

$$B'_p \approx (5 \times 10^7\,\mathrm{G})\ R_{13.65}^{-2/3}\ \Gamma_{0,900}\ h\nu_{\mathrm{obs},300}^{-1/3}, \tag{8}$$

which would require a high (collimation-corrected) Poynting flux (see Florou et al. 2021):

$$P_{B,p} \approx (5 \times 10^{54}\,\mathrm{erg\,s^{-1}})\ \theta_{j,1_\circ}^2\ B_{7.72}^2\ \Gamma_{0,900}^2 R_{13.65}^2. \tag{9}$$

In the estimates mentioned above we have assumed that the GRB spectrum arises from marginally fast cooling electrons/protons. If we relax this requirement, i.e., assume that $t_{\mathrm{syn}} \geqslant R/2c\Gamma_0^2$, then our estimates on B' would be only upper limits.

Nonetheless, it is expected that, in the assumption of electrons and protons injected with the same Lorenz factor distribution, the electron–synchrotron component luminosity would be smaller by a factor m_p/m_e, allowing us to neglect this contribution (Ghisellini et al. 2020).

This scenario does not include the contribution that electrons can have in the overall spectrum through synchrotron cooling, and possibly SSC and IC with the proton–synchrotron photons. Deeper investigations of the role of electrons in the proton–

synchrotron scenario are required to assess its capability of explaining current observations (see Bégué et al. 2021; Florou et al. 2021) We also notice that the observed luminosity of GRB 220101A and the constrained values of R_γ and Γ_0 suggest that the proton–synchrotron emission dominates over the synchrotron emission from the Bethe–Heitler pairs (Bégué et al. 2021).

Moreover, it is consistent with the low-energy spectral shape of GRB 220101A, $\alpha = 0.70$, and the adiabatic cooling inferred from the X-ray decline of the prompt emission pulses (Ronchini et al. 2021). In this scenario, the GRB-emitting particles (protons) do not cool efficiently in a dynamical timescale, and the GRB variability is given purely by the adiabatic expansion time, i.e., $R/2c\Gamma_0^2$. Clearly, this corresponds to very low prompt emission efficiency, leaving most of the energy to dissipate in the afterglow phase. However, electrons will lose all their energy given large magnetic fields, producing both high-energy and very high energy (VHE) emissions. In this scenario, what we observe as a GRB at the keV–MeV range is only adiabatically cooling proton emission. Ghisellini et al. (2020) showed that if electrons and protons have the same Lorentz factor distribution, then we would expect an emission component at $h\nu_{\mathrm{obs}} \approx 0.5\,\mathrm{GeV}\ h\nu_{\mathrm{obs},300}$ with a luminosity of $L_{\mathrm{iso}} \approx 2 \times 10^{50}\,\mathrm{erg\,s^{-1}}$. In the case of electrons and protons sharing the same energy distribution, we would expect the electron–synchrotron component to peak at 2×10^{15} eV with the same proton–synchrotron luminosity. In the latter case, one should carefully take into account the pair cascade caused by these extremely high energy photons. Nevertheless, the observations of the GRB prompt emission spectra at high and very high energies could be a powerful tool to discriminate the GRB emission models and to constrain the acceleration processes by identifying the relative proton-to-electron energy ratio.

We want to stress the fact that the conclusions of this work are drawn within the framework of the synchrotron model. We do not discuss the implication of a subphotospheric emission (Rees & Mészáros 2005; Pe'er 2008), magnetic reconnection in

a highly magnetized ejecta (Zhang & Yan 2011), or hybrid jets (Gao & Zhang 2015). Despite this, it is worth mentioning that the most stringent constraints we find in the $R_\gamma - \Gamma$ plane are driven from observations, not requiring any prior assumption on the prompt physics.

In this work we analyze one of the most energetic GRBs ever observed. Estimated from the KW detection (GCN 31433), the burst E_{iso} is $3.64^{+0.25}_{-0.22} \times 10^{54}$ erg, which is within the highest $\sim 2\%$ for the KW sample of 338 GRBs with known redshifts (Tsvetkova et al. 2017, 2021). With this E_{iso} and the rest-frame peak energy of 1416^{+152}_{-157} keV, GRB 220101A is within 68% prediction bands for the Amati relation for the same sample of long KW GRBs with known redshifts.

The joint spectral and temporal analysis of the source shows the presence of the afterglow emission in the X-ray and high-energy bands from 118 s. The measured cutoff energy $E_{cutoff} = 85^{+16}_{-26}$ MeV and minimum afterglow observations were revealed to be powerful tools to constrain the dynamics and dimension of the prompt emitting region, leading to the stringent constraints on $\log R_\gamma \text{[cm]} = 13.7^{+0.6}_{-0.4}$ and $700 < \Gamma_0 < 1160$, in favor of a proton–synchrotron scenario rather than an electron–synchrotron one. The inferred radius of the prompt emission is above the jet photosphere and below the typical magnetic reconnection regions.

More observations in the MeV–GeV and VHE domains are necessary to fully uncover the physics of the GRB jet dissipation and acceleration processes.

Appendix A
Data

A.1. Swift/XRT

We have downloaded the data provided by XRT (0.5–10 keV) on board Swift from the Swift Science Data Center supported by the University of Leicester (Evans et al. 2009). Nine time bins (93–3788 s from the GRB trigger time) in the Window Timing mode and 18 time bins ($4 \times 10^3 - 6 \times 10^5$ s) in the Photon Counting mode were selected for the time-resolved spectral analysis to evaluate the temporal and spectral evolution of the X-ray emission during the prompt and afterglow phases. Additional spectra at the early times are retrieved to perform joint Fermi/GBM, Fermi/LAT, Swift/ BAT, and KW analysis. The choice of the time intervals was driven by the significant Fermi/LAT detection. We adopt Cash statistics to fit XRT spectra.

A.2. Swift/BAT

The data from BAT (15–150 keV) were downloaded from the Swift data archive. The FTOOLS `batmaskwtevt` and `batbinevt` pipelines are used to extract the background-subtracted mask-weighted BAT light curves. To produce BAT spectra and the corresponding response files, we have used the `batbinevt` task, together with the `batupdatephakw`, `batphasyserr`, and `batdrmgen` tools. We have applied Gaussian statistics to fit the BAT spectra.

A.3. Konus-Wind

KW (Aptekar et al. 1995) is a γ-ray spectrometer consisting of two identical NaI(Tl) detectors, S1 and S2, which observe the southern and northern ecliptic hemispheres, respectively. Each detector has an effective area of 80–160 cm^2, depending on the photon energy and incident angle, and collects the data in the $\sim$20 keV–20 MeV energy range. GRB 220101A triggered the S2 detector of the KW at $T_0(KW) = 05:11:35.828$ UT. For this burst, the triggered mode light curves are available, starting from $T_0(KW)$-0.512 s, in three energy windows G1 ($\sim$20–80 keV), G2 ($\sim$80–330 keV), and G3 ($\sim$330–1320 keV), with time resolution varying from 2 up to 256 ms and a total record duration of $\sim$230 s. The burst spectral data are available, starting from $T_0(KW)$, in two overlapping energy intervals, PHA1 (20–1300 keV) and PHA2 (270 keV–16 MeV). The total duration of the spectral measurements is $\sim$490 s. The KW background is very stable and assumed to be at a constant level during the triggered mode record. For GRB 220101A (Tsvetkova 2022; Tsvetkova et al. 2022), we constructed the background spectrum as a sum of spectra outside the burst emission episodes, from $\sim T_0(KW)+205$ s to $\sim T_0(KW)+435$ s. With $>$100 counts per energy channel, the background is assumed to be Gaussian, and the errors are computed as a square root of the channel counts. When fitting the KW data, the χ^2 statistics is typically applied to the spectra grouped to have a minimum of 20 counts per energy bin, or pgstat can be used with the data grouped to a minimum of 1 count per bin. In the latter case, cstat can also be used, which yields nearly the same results as pgstat. A more detailed description of the KW data and the data reduction procedures can be found, e.g., in Svinkin et al. (2016) and Tsvetkova et al. (2017, 2021).

A.4. Fermi/GBM

We have selected two sodium iodide (NaI, 8–900 keV) detectors, namely NaI-6 and NaI-7, and one bismuth germanate (BGO, 0.3–40 MeV) detector BGO-1 to retrieve the data from the GBM on board Fermi. Fermi/GBM data are extracted by the GTBURST tool. We have excluded the energy bins below 8 keV and above 900 keV for NaI detectors and below 300 keV and above 10 MeV for the BGO-1 detector. To fit the Fermi/ GBM spectra, we have applied the PGSTAT likelihood.

A.5. Fermi/LAT

Fermi/LAT is sensitive to the gamma-ray photons of energy between 30 MeV and 300 GeV (Ackermann et al. 2013). We use the GTBURST tool to extract and analyze the data. The source (R.A. = 1°.35 and decl. = 31°.77) was inside the field of view of LAT until around 1400 s after the trigger. For this analysis, we use a region of interest of 12° centered at the burst position provided by Swift/BAT (Tohuvavohu et al. 2022). As the spectral model, particle background, and Galactic component we assume "`powerlaw2`," "`isotr template`," and "`template (fixed norm.)`," respectively. The estimation of flux in the energy between 100 MeV and 10 GeV is performed with the "`unbinned likelihood analysis`."

Due to the low statistics in the Fermi/LAT temporal bins, we cannot perform a binned likelihood analysis. The highest energy of the photon associated with GRB 220101A has energy of 930 MeV at 150 s from the GRB trigger time. Most of the photons have energies between 100 and 250 MeV and are detected during the main prompt emission episode (observed by BAT, GBM, and KW). The time bins for the joint spectral analysis were chosen requiring significant Fermi/LAT detections (minimum test statistics TS > 10). No LAT low-energy events (LLE) data are available for this burst. We generate an LAT count spectrum through GTBURST using the Standard ScienceTool[9] pipeline gtbin. In addition, we produce the background counts and response files using gtbkg and gtrspgen, respectively (e.g., Ajello et al. 2020). We fit the LAT spectrum on XSPEC using Cash statistics.

A.6. Optical Data

GRB 220101A has been followed up by numerous optical telescopes. We have selected the r-band observations (AB system) from the GCN Circulars Archive to use single-filter homogeneous optical data for the afterglow modeling. We ignore the early optical detection by Swift/UVOT at ~150 s (Kuin & Tohuvavohu 2022), since the single bright optical detection is not informative enough to discriminate between the forward and reverse shock contributions. We include in the analysis data from the Liverpool telescope (Perley 2022a, 2022b), the Tautenburg 1.34 m Schmidt telescope (Nicuesa Guelbenzu et al. 2022), the

CAFOS instrument (Caballero-Garcia et al. 2022), and the Konkoly Observatory (Vinko et al. 2022).

Appendix B
Markov Chain Monte Carlo

B.1. Prompt Fit

We performed a joint spectral fit of XRT+BAT+GBM+KW+LAT data during the *prompt* time bin (94–118 s), which is described by a Band function with a cutoff at $E_{cutoff} \simeq 80$ MeV. For the *Band+cutoff* model, we performed an MCMC to sample the posterior distribution of the fitted parameters, using the XSPEC task chain.

This analysis returns, for each model parameter, a chain of parameter values whose density gives the parameter probability distribution. We employ the Goodman–Weare algorithm, requiring $N_{walkers} = 4$ walkers and $N_{iter} = 10^6$ iterations. Since the starting parameters are far from convergence, we ignore the first $N_{burn} = 5 \times 10^4$ steps. The walkers are initialized by drawing from a multi-Normal distribution whose variance matrix is based on the covariance matrix obtained from the previous XSPEC fit. The parameter contours obtained from the prompt MCMC are shown in Figure 6.

B.2. Afterglow Fit

We fit six afterglow parameters using an MCMC approach, namely the isotropic equivalent kinetic energy of the jet E_{kin}, the opening angle of the jet θ_j, the circumburst medium density
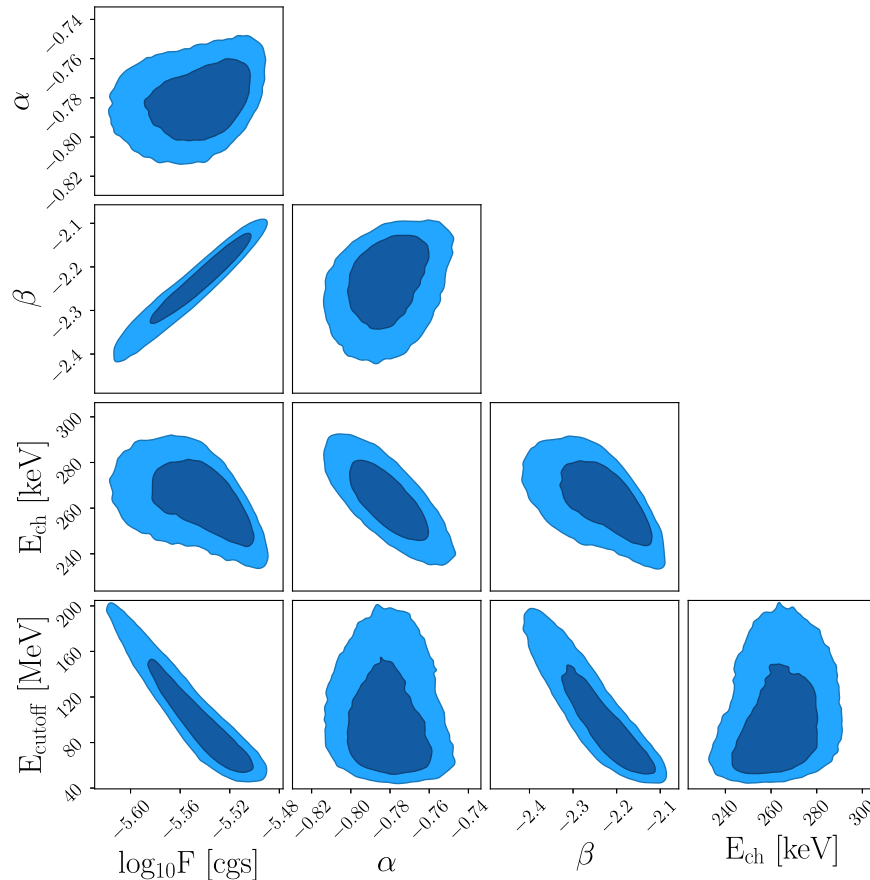

Figure 6. Corner plot showing the parameter contours obtained from the MCMC of the prompt fit parameters, namely the low- and high-energy slopes α and β, respectively, the characteristic energy E_{ch}, the cutoff energy E_{cutoff}, and the flux integrated between 0.1 keV and 0.25 GeV. The 1σ contour region is shown in dark blue, while in light blue we show the 2σ contour region.
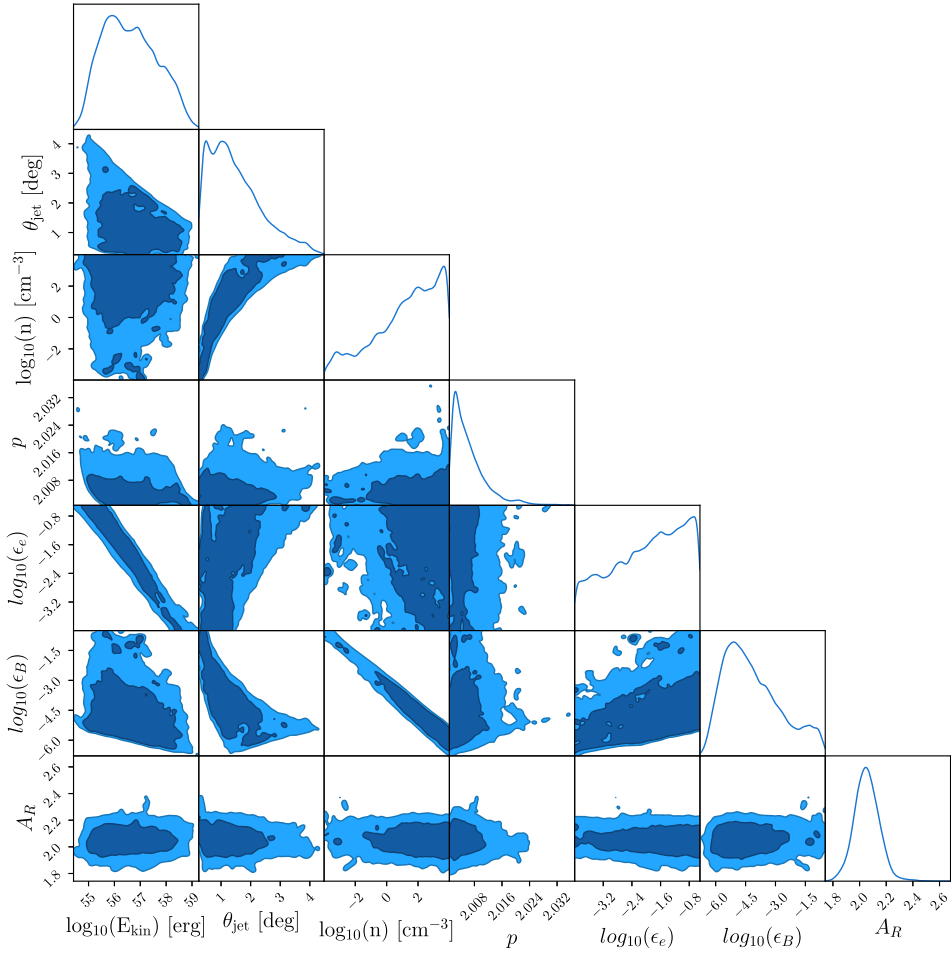
Figure 7. Corner plot showing the parameter marginalized posterior distributions and contours from the MCMC performed for the afterglow analysis. The best-fit values and priors are shown in Table 2. The parameters fitted in the MCMC are the isotropic equivalent energy $E_{\rm kin}$, the jet opening angle θ_j, the circumburst medium density n, the electron distribution index p, absorption of optical emission A_R, and the constant fraction of the shock energy that goes to electrons ϵ_e and into magnetic energy density ϵ_B.

n, electron distribution index p, the constant fraction of the shock energy that goes into electrons ϵ_e and into the magnetic energy density ϵ_B, and the absorption of the optical emission A_R.

Our observables are the flux density estimates measured in the optical, X-ray, and γ-ray band $F_{\nu,i}$ and the photon indexes in the X-ray and γ-ray band α_i. Each observable $\theta_i \in \{F_i, \alpha_i\}$ contributes to the overall log-likelihood with an additive term, given by

$$\log L_i = -\frac{1}{2} \frac{(\theta_{m,i} - \theta_i)^2}{\sigma_{\theta,i}^2} - \frac{1}{2} \ln(\sigma_{\theta,i}^2), \qquad (B1)$$

where $\theta_{m,i}$ is the observable predicted by the model and $\sigma_{\theta,i}$ is the associated uncertainty. Since GRB 220101A is particularly luminous and we do only observe the decaying phase of the afterglow, it is safe to assume that it is on-axis. Therefore, we employ an analytical model based on self-similar adiabatic afterglow solutions (Granot & Sari 2002; Gao et al. 2013) to predict fluxes and photon indexes. We adopt log-uniform priors for $E_{\rm kin}$, n, ϵ_e, and ϵ_B and uniform priors for p, θ_j, and A_R (see Table 2).

We sample the posterior probability density through MCMC using the EMCEE Python package (Foreman-Mackey et al. 2013), employing $N_{\rm walk} = 12$ walkers for $N_{\rm iter} = 500{,}000$ iterations. The prior used for the MCMC and the results of the fit are reported in Table 2, while the corner plot with marginalized posterior distributions for each parameter is shown in Figure 7.

ORCID iDs

Alessio Mei ⓘ https://orcid.org/0000-0003-1324-5296
Gor Oganesyan ⓘ https://orcid.org/0000-0001-9765-1552
Anastasia Tsvetkova ⓘ https://orcid.org/0000-0003-0292-6221
Maria Edvige Ravasio ⓘ https://orcid.org/0000-0003-3193-4714
Biswajit Banerjee ⓘ https://orcid.org/0000-0002-8008-2485
Samuele Ronchini ⓘ https://orcid.org/0000-0003-0020-687X
Marica Branchesi ⓘ https://orcid.org/0000-0003-1643-0526

References

Ackermann, M., Ajello, M., Allafort, A., et al. 2013, ApJS, 209, 34
Acuner, Z., Ryde, F., Pe'er, A., Mortlock, D., & Ahlgren, B. 2020, ApJ, 893, 128
Ajello, M., Arimoto, M., Axelsson, M., et al. 2020, ApJ, 890, 9
Algeri, S., Aalbers, J., Mora, K. D., & Conrad, J. 2020, NatRP, 2, 245

Aptekar, R. L., Frederiks, D. D., Golenetskii, S. V., et al. 1995, SSRv, 71, 265
Band, D., Matteson, J., Ford, L., et al. 1993, ApJ, 413, 281
Bégué, D., Samuelsson, F., & Pe'er, A. 2021, ApJ, 937, 101
Beniamini, P., Nava, L., Duran, R. B., & Piran, T. 2015, MNRAS, 454, 1073
Beniamini, P., & Piran, T. 2013, ApJ, 769, 69
Burgess, J. M., Begue, D., Greiner, J., et al. 2020, NatAs, 4, 174
Burgess, J. M., Preece, R. D., Connaughton, V., et al. 2014, ApJ, 784, 17
Caballero-Garcia, M. D., Sanchez-Ramirez, R., Hu, Y. D., et al. 2022, GCN, 31388, 1
Chand, V., Pal, P. S., Banerjee, A., et al. 2020, ApJ, 903, 9
Daigne, F., & Mochkovitch, R. 2002, MNRAS, 336, 1271
Drenkhahn, G., & Spruit, H. C. 2002, A&A, 391, 1141
Evans, P. A., Beardmore, A. P., Page, K. L., et al. 2009, MNRAS, 397, 1177
Florou, I., Petropoulou, M., & Mastichiadis, A. 2021, MNRAS, 505, 1367
Foreman-Mackey, D., Hogg, D. W., Lang, D., & Goodman, J. 2013, PASP, 125, 306
Gao, H., Lei, W.-H., Zou, Y.-C., Wu, X.-F., & Zhang, B. 2013, NewAR, 57, 141
Gao, H., & Zhang, B. 2015, ApJ, 801, 103
Ghirlanda, G., Nava, L., Ghisellini, G., et al. 2012, MNRAS, 420, 483
Ghirlanda, G., Nappo, F., Ghisellini, G., et al. 2018, A&A, 609, A112
Ghisellini, G., Ghirlanda, G., Nava, L., & Celotti, A. 2010, MNRAS, 403, 926
Ghisellini, G., Ghirlanda, G., Oganesyan, G., et al. 2020, A&A, 636, A82
Gill, R., Granot, J., & Beniamini, P. 2020, MNRAS, 499, 1356
Granot, J., Cohen-Tanugi, J., & Silva, E. d. e. 2008, ApJ, 677, 92
Granot, J., & Sari, R. 2002, ApJ, 568, 820
Guilbert, P. W., Fabian, A. C., & Rees, M. J. 1983, MNRAS, 205, 593
Gupta, N., & Zhang, B. 2008, MNRAS, 384, L11
Hascoët, R., Daigne, F., Mochkovitch, R., & Vennin, V. 2012, MNRAS, 421, 525
Kuin, N. P. M., Tohuvavohu, A. & Swift/UVOT Team 2022, GCN, 31351, 1
Kumar, P., & Duran, R. B. 2010, MNRAS, 409, 226
Kumar, P., Hernández, R. A., Bošnjak, Ž., & Barniol Duran, R. 2012, MNRAS, 427, L40
Kumar, P., & McMahon, E. 2008, MNRAS, 384, 33
Kumar, P., & Zhang, B. 2015, PhR, 561, 1
Lithwick, Y., & Sari, R. 2001, ApJ, 555, 540
Lloyd, N. M., & Petrosian, V. 2000, ApJ, 543, 722
Lü, J., Zou, Y.-C., Lei, W.-H., et al. 2012, ApJ, 751, 49
Mészáros, P., & Rees, M. J. 1997, ApJ, 476, 232
Nakar, E., Ando, S., & Sari, R. 2009, ApJ, 703, 675
Nava, L. 2018, IJMPD, 27, 1842003
Nava, L., Desiante, R., Longo, F., et al. 2017, MNRAS, 465, 811
Nava, L., Sironi, L., Ghisellini, G., Celotti, A., & Ghirlanda, G. 2013, MNRAS, 433, 2107
Nicuesa Guelbenzu, A., Melnikov, S., Klose, S., Stecklum, B., & Ludwig, F. 2022, GCN, 31401, 1
Oganesyan, G., Nava, L., Ghirlanda, G., & Celotti, A. 2017, ApJ, 846, 137
Oganesyan, G., Nava, L., Ghirlanda, G., & Celotti, A. 2018, A&A, 616, A138
Oganesyan, G., Nava, L., Ghirlanda, G., Melandri, A., & Celotti, A. 2019, A&A, 628, A59
Paczynski, B., & Rhoads, J. E. 1993, ApJL, 418, L5
Pe'er, A. 2008, ApJ, 682, 463
Perley, D. A. 2022a, GCN, 31357, 1
Perley, D. A. 2022b, GCN, 31425, 1
Piran, T. 1999, PhR, 314, 575
Piran, T. 2004, RvMP, 76, 1143
Ravasio, M. E., Ghirlanda, G., Nava, L., & Ghisellini, G. 2019, A&A, 625, A60
Rees, M. J., & Meszaros, P. 1994, ApJL, 430, L93
Rees, M. J., & Mészáros, P. 2005, ApJ, 628, 847
Ronchini, S., Oganesyan, G., Branchesi, M., et al. 2021, NatCo, 12, 4040
Ruderman, M. 1975, in Seventh Texas Symp. on Relativistic Astrophysics, ed. P. G. Bergman, E. J. Fenyves, & L. Motz, Vol. 262 (New York: Annals of the New York Academy of Sciences), 164
Sari, R., & Piran, T. 1999, ApJ, 520, 641
Sari, R., Piran, T., & Narayan, R. 1998, ApJL, 497, L17
Svensson, R. 1987, MNRAS, 227, 403
Svinkin, D. S., Frederiks, D. D., Aptekar, R. L., et al. 2016, ApJS, 224, 10
Tavani, M. 1996, ApJ, 466, 768
Tohuvavohu, A., Gropp, J. D., Kennea, J. A., et al. 2022, GCN, 31347, 1
Tsvetkova, A. 2022, GCN, 31436, 1
Tsvetkova, A., Frederiks, D., Golenetskii, S., et al. 2017, ApJ, 850, 161
Tsvetkova, A., Frederiks, D., Lysenko, A., et al. 2022, GCN, 31433, 1
Tsvetkova, A., Frederiks, D., Svinkin, D., et al. 2021, ApJ, 908, 83
Vianello, G., Gill, R., Granot, J., et al. 2018, ApJ, 864, 163
Vinko, J., Pal, A., Kriskovics, L., Szakats, R., & Vida, K. 2022, GCN, 31361, 1
Yu, H.-F., Greiner, J., van Eerten, H., et al. 2015, A&A, 573, A81
Zhang, B. 2020, NatAs, 4, 210
Zhang, B., & Pe'er, A. 2009, ApJL, 700, L65
Zhang, B., & Yan, H. 2011, ApJ, 726, 90
Zou, Y.-C., Fan, Y.-Z., & Piran, T. 2011, ApJL, 726, L2